This is a preprint, the final version is subject to change, of the American Mineralogist (MSA)
Cite as Authors (Year) Title. American Mineralogist, in press.
DOI: https://doi.org/10.2138/am-2020-7333

Revision 1

Interlayer energy of pyrophyllite: Implications for macroscopic friction

Hiroshi Sakuma[1], Kenji Kawai[2], and Toshihiro Kogure[2]

[1]*Functional Clay Materials Group, National Institute for Materials Science, Tsukuba, Japan*

[2]*Department of Earth and Planetary Science, School of Science, University of Tokyo, Tokyo, Japan*

Corresponding author: H. Sakuma (SAKUMA.Hiroshi@nims.go.jp)

Running title: Interlayer energy of pyrophyllite

This is a preprint, the final version is subject to change, of the American Mineralogist (MSA)
Cite as Authors (Year) Title. American Mineralogist, in press.
DOI: https://doi.org/10.2138/am-2020-7333

Revision 1

Abstract

Deformation of phyllosilicate can control the dynamics of the Earth's crust. The phenomenological relationship between stress and deformation is known for some typical phyllosilicates; however, the underlying physics originating from the crystal structures is poorly understood. In this study, the deformation mechanism of pyrophyllite along basal planes was revealed through density functional theory calculations and atomic-scale theory of friction. The stable and meta-stable interlayer structures formed by interlayer slide were consistent with the experimental results reported previously by high resolution transmission electron microscopy. The difference in potential energies between stable and meta-stable interlayer structures can be interpreted as the difference in stacking of dioctahedral sheets between the adjacent layers. The estimated friction coefficient of the pyrophyllite between adjacent layers was consistent with the results of atomic force microscopy, suggesting that atomic-scale friction can be adequately estimated by this method. The calculated shear stress in our simulations has a linear relationship with the normal stress and has no significant crystallographic dependence on sliding direction along the basal planes. The crystallographic isotropy of interlayer friction is explained by the absence of interlayer cations in pyrophyllite, while muscovite showed crystallographic anisotropy as observed in

previous studies. The macroscopic friction of a single crystal of pyrophyllite was estimated from atomic-scale friction by using the area of contact. The macroscopic friction coefficient of ideal interlayer sliding was estimated to be 0.134, which was smaller than a reported value (0.276) in shear experiments conducted for wet polycrystalline gouge layers. This difference can be primarily explained by the degree of orientation of pyrophyllite particles in the gouge layers. The friction coefficient estimated by a simple model of randomly oriented pyrophyllite gouge layer was 0.203 ± 0.001, which was similar to the reported value of 0.276 and clearly smaller than the values (0.6–0.85) of common minerals estimated by the empirical Byerlee's law. These results indicate that weak interlayer friction of phyllosilicates has a large effect on the low frictional strength of gouge layers in natural faults. Our methodology and results are useful for understanding the physics behind the phenomenological friction laws of phyllosilicate gouge. **Keywords:** pyrophyllite, friction coefficient, interlayer friction, gouge layers, density functional theory

This is a preprint, the final version is subject to change, of the American Mineralogist (MSA)
Cite as Authors (Year) Title. American Mineralogist, in press.
DOI: https://doi.org/10.2138/am-2020-7333

Revision 1

Introduction

Deformation of rocks and minerals controls crustal dynamics. The shear strength of rocks can be reduced by the presence of phyllosilicates (Byerlee 1978; Shea and Kronenberg 1993; Wintsch et al. 1995; Jefferies et al. 2006; Mariani et al. 2006; Amiguet et al. 2012). Phyllosilicates have been found in many natural faults and on sliding planes of landslides; therefore, the frictional properties of phyllosilicates are critical for understanding the dynamics of the Earth's crust.

The stability of gouge-bearing faults have been evaluated in a laboratory using shear tests and through analyses based on a phenomenological rate- and state-dependent friction (RSF) law (Dieterich 1979; Ruina 1983); however, the physics behind the law depends on the materials, is complicated, and it is difficult to extrapolate the results to natural faults. Grain boundary friction, grain-size reduction, grain rolling, and pressure solution are critical parameters effecting granular fault gouges (Bos and Spiers 2001). Recent development of a microphysical model partly reveals the physics behind the macroscopic frictional strength of granular fault gouges (Chen and Spiers 2016; Chen et al. 2017). In their model, the shear strength of the gouge is mainly controlled by porosity and grain boundary friction. However, the model was limited to spherical particles and grain

This is a preprint, the final version is subject to change, of the American Mineralogist (MSA)
Cite as Authors (Year) Title. American Mineralogist, in press.
DOI: https://doi.org/10.2138/am-2020-7333

boundary friction was still expressed by an empirical parameter.

Grain boundary friction of phyllosilicates may be weaker than for other minerals because of two reasons. First, friction can be lubricated by adsorbed and interlayer water in hydrophilic phyllosilicates (Horn and Deere 1962; Morrow et al. 2000; Sakuma et al. 2006; Ikari et al. 2007; Moore and Lockner 2007; Sakuma et al. 2011; Behnsen and Faulkner 2012; Sakuma 2013; Katayama et al. 2015; Kawai et al. 2015; Morrow et al. 2017; Tetsuka et al. 2018). Second, the presence of weak bonding planes in phyllosilicate crystal structures can reduce the frictional force (Moore and Lockner 2004; Kawai et al. 2015; Sakuma et al. 2018; Okuda et al. 2019).

Here, we focused on the second hypothesis during dry conditions by studying hydrophobic pyrophyllite minerals. Recent experimental and theoretical calculations revealed that sub-meter scale frictional strength of a single muscovite crystal along basal planes can be explained by the roughness of the atomic-scale potential energy surface during sliding (Sakuma et al. 2018). The potential energy should depend on the crystal structures; therefore, this mechanism should be tested on various phyllosilicates and sheet-structured minerals. A theoretical calculation of brucite revealed the difference between interlayer friction with muscovite, which would originate from the differences in

This is a preprint, the final version is subject to change, of the American Mineralogist (MSA)
Cite as Authors (Year) Title. American Mineralogist, in press.
DOI: https://doi.org/10.2138/am-2020-7333

interlayer interactions (Okuda et al. 2019).

Pyrophyllite is a 2:1 type dioctahedral clay mineral and the charge of the layer is neutral. The interlayer bonding energy is characterized by weak van der Waals forces, in contrast to the relatively strong Coulomb forces of micas and hydrogen bonding in hydroxides (Sakuma and Suehara 2015). During atomic-scale friction, a low friction coefficient was observed between a silicon nitride tip and pyrophyllite flakes by using atomic force microscopy (Bucholz et al. 2012). For macroscopic friction under a confining pressure of 100 MPa, the maximum friction coefficient of pyrophyllite was 0.4 for highly aligned pyrophyllite grains within shear planes, while muscovite had a value of 0.55 (Moore and Lockner 2004). It would be difficult to determine the relationship between atomic-scale and macroscopic friction only from these previous studies, because of non-negligible effects of the silicon nitride tip on atomic-scale friction.

Here the change in potential energy of pyrophyllite along six sliding paths on a basal plane was calculated based on the density functional theory (DFT) (Hohenberg and Kohn 1964; Kohn and Sham 1965). The reliability of the DFT calculations were confirmed by comparing the stable and meta-stable structures with high-resolution transmission electron microscopy (HRTEM) observations (Kogure et al. 2006; Kogure and Kameda 2008). The

This is a preprint, the final version is subject to change, of the American Mineralogist (MSA)
Cite as Authors (Year) Title. American Mineralogist, in press.
DOI: https://doi.org/10.2138/am-2020-7333

93 frictional strength of a single pyrophyllite crystal determined using DFT calculations are
94 discussed and the results were used to understand the origin of macroscopic deformation of
95 pyrophyllite in a frictional regime.
96
97 **Computational methods**
98 **Potential energy surface and frictional force**
99 Atomic-scale friction can be estimated from the roughness of the potential energy
100 surface during sliding (Zhong and Tománek 1990; Schwarz and Hölscher 2016; Sakuma et
101 al. 2018). The computational method to obtain the potential energy profile along a sliding
102 path is the same as in previous studies (Zhong and Tománek 1990; Sakuma et al. 2018).
103 Briefly, the interlayer energy E_{IL} as a function of sliding distance x and interlayer distance z
104 was calculated as follows.
105
106 $$E_{\mathrm{IL}}(x,z) = E_{\mathrm{2layers}}(x,z) - 2E_{\mathrm{1layer}} \quad (1)$$
107
108 Here, E_{2layers} and E_{1layer} are the total energy of two pyrophyllite layers and the single layer in
109 the supercell, respectively. The interlayer distance z depends on the applied load f_{ext} as

This is a preprint, the final version is subject to change, of the American Mineralogist (MSA)
Cite as Authors (Year) Title. American Mineralogist, in press.
DOI: https://doi.org/10.2138/am-2020-7333

follows.

$$f_{\mathrm{ext}} = -\frac{\partial E_{\mathrm{IL}}(x,z)}{\partial z} \qquad (2)$$

Potential energy V as a function of x and f_{ext} can be obtained by considering the interlayer energy and the work against the applied load as follows.

$$V(x, f_{\mathrm{ext}}) = E_{\mathrm{IL}}(x, z) + f_{\mathrm{ext}} z \quad (3)$$

The potential energy difference is only required for calculating the frictional force; therefore, V was expressed as the difference from the minimum potential energy in this study. The frictional force f_{friction} as a function of x and f_{ext} can be obtained by the derivative with respect to x of the potential energy as follows.

$$f_{\mathrm{friction}}(x, f_{\mathrm{ext}}) = \frac{\partial V}{\partial x} \qquad (4)$$

To obtain the frictional force, the potential energy surface can be estimated from

This is a preprint, the final version is subject to change, of the American Mineralogist (MSA)
Cite as Authors (Year) Title. American Mineralogist, in press.
DOI: https://doi.org/10.2138/am-2020-7333

DFT calculations.

Density functional theory calculations

The relaxed structure and potential energies of pyrophyllite layers under shear were derived from the DFT calculations. The exchange and correlation energy were calculated using the generalized gradient approximation of the Perdew-Burke-Ernzerhof (GGA-PBE) method (Perdew et al. 1996). Valence electrons in atoms were explicitly considered in the calculations using a pseudopotential method (Garrity et al. 2014). A semiempirical dispersion force correction (DFT-D2) (Grimme 2006; Barone et al. 2009) was included in the calculations for reproducing weak van der Waals forces among atoms. The reliability of the corrections were confirmed in our previous study by comparing the results with several dispersion-correction methodologies (Sakuma and Suehara 2015). All DFT calculations were performed using QUANTUM ESPRESSO (Giannozzi et al. 2009, 2017).

Bulk calculations. To test the reliability of the employed computational method, pyrophyllite lattice constants were calculated under various input parameters in DFT calculations. The initial structure of pyrophyllite was set to that reported by an X-ray

This is a preprint, the final version is subject to change, of the American Mineralogist (MSA)
Cite as Authors (Year) Title. American Mineralogist, in press.
DOI: https://doi.org/10.2138/am-2020-7333

144 diffraction (XRD) method (Lee and Guggenheim 1981). The supercell includes 40 ions
145 composed of two $Al_2(Si_4O_{10})(OH)_2$ units. Convergence thresholds on the total ion energies
146 in the supercell, forces, and stresses were 1×10^{-6} Ry (=0.0136 meV), 1×10^{-4} Ry/bohr/ion
147 (=1.36 meV/bohr/ion), and 0.5 kbar, respectively. Kinetic energy cutoffs for wavefunction
148 and charge density were chosen to be 40 Ry (=544.2 eV) and 320 Ry (= 4353.6 eV),
149 respectively, by confirming the energy and structural convergences. These cutoff energies
150 were fixed for subsequent calculations on slab geometry. Sampling of k-points in the
151 Brillouin zone was established using 4 × 2 × 2 in Monkhorst-Pack grids (Monkhorst and
152 Pack 1976), which was sufficient to achieve energy and structural convergences.
153 **Slab calculations.** Interlayer energy was calculated using the total energy of two layers in
154 the supercell subtracted by two single layers in the supercell, as calculated in our previous
155 studies (Sakuma and Suehara 2015; Sakuma et al. 2017, 2018). The size of the supercell
156 was determined to be a = 5.17539 Å, b = 8.98879 Å, c = 46.78165 Å, α = 90.97º, β =
157 100.58º, and γ = 89.83º based on the relaxed structures in bulk calculations, except for
158 length c. Length c was elongated to include vacuum space. Sampling of k-points in the
159 Brillouin zone was set to 4 × 2 × 1 in Monkhorst-Pack grids. A dipole correction
160 (Bengtsson 1999) was applied perpendicular to the basal plane of pyrophyllite to remove an

This is a preprint, the final version is subject to change, of the American Mineralogist (MSA)
Cite as Authors (Year) Title. American Mineralogist, in press.
DOI: https://doi.org/10.2138/am-2020-7333

161 artifact arising from periodic boundary conditions. In this supercell, the size of *a*-*b* plane
162 was equal to the area in only one crystallographic unit cell. A comparison of calculated
163 elastic constants and shear modulus with experimental values may be a clue for
164 understanding the effect of system size, though it is difficult to obtain precise values in
165 experiments. A DFT study on kaolinite (Weck et al. 2015) revealed that calculated shear
166 constants and shear modulus using a small supercell of a = 5.18 Å, b = 8.98 Å, and c = 7.33
167 Å were consistent with experiments. These results imply that the small system size used in
168 our study has insignificant effect on shear deformation. Atomic relaxations were
169 conducted for ions in the supercell except Al ions in octahedral sites. Fixing the position of
170 these Al ions is required to fix the interlayer distance. Convergence thresholds on the total
171 ion energies in the supercell and forces were 1×10^{-6} Ry (=0.0136 meV) and 1×10^{-4}
172 Ry/bohr/ion (=1.36 meV/bohr/ion), respectively.
173

174 **Results and discussion**

175 **The bulk structure of pyrophyllite**

176 Calculated lattice constants of pyrophyllite are listed in Table 1. The differences
177 between and the calculated and experimental lattice constants were less than 0.3% for all

This is a preprint, the final version is subject to change, of the American Mineralogist (MSA)
Cite as Authors (Year) Title. American Mineralogist, in press.
DOI: https://doi.org/10.2138/am-2020-7333

parameters.

Interlayer energy along six sliding paths

Six sliding paths parallel to the basal plane were tested by considering crystallographic symmetry as shown in Fig 1. The length of sliding paths L depends on the sliding directions, because crystallographic equivalent positions to the initial positions are required for averaging the frictional forces. The interlayer energies E_{IL} were calculated every ~0.5 Å along the paths. The results along path 1 are shown in Fig. 2. Horizontal sliding of the top layers can be confirmed by analyzing the top views of the interfacial tetrahedral sheets. The triangle indicating the same SiO_4 tetrahedron in the top layer moved from left to right along path 1 as shown in Figs. 2 (A), (B), and (C). The interlayer energy was calculated at various x displacements in the top layer by moving the top layer up and down perpendicular to the basal plane as shown in Fig. 2 (D). The interlayer energies at various x's were plotted in Fig. 2 (E). The lowest energy was obtained at $x = 0$ which corresponds to the stacking structure reported by the single-crystal X-ray measurements of pyrophyllite (Lee and Guggenheim 1981). The energy increased as the two layers approached each other indicating the repulsion between the layers. The z positions of lowest energies in the profiles changed depending on the displacement x. The interlayer

This is a preprint, the final version is subject to change, of the American Mineralogist (MSA)
Cite as Authors (Year) Title. American Mineralogist, in press.
DOI: https://doi.org/10.2138/am-2020-7333

195 energies were fitted to an eighth- or seventh-degree polynomial equation and analytically
196 calculated derivatives were used to derive the *z* position balanced with applied normal
197 forces. All interlayer energies along the six sliding paths are available in the supplemental
198 figure S1.

199 **Potential energy profiles along six sliding paths and experimentally observed**
200 **interlayer structures**

201 Potential energy changes along six sliding paths are plotted in Fig. 3. The difference
202 between the lowest and highest potential energies increased as the applied normal stress σ_n
203 increased from 0 to 10.7 GPa. The most common interlayer structures determined by XRD
204 measurements correspond to the lowest potential energy at x = 0 and σ_n = 0 GPa for all
205 sliding paths. Similar low potential energy configurations were derived for paths 1, 3, and 5
206 at x = 3.1, 5.9, and 2.8 Å, respectively. Several meta-stable configurations appeared for
207 paths 1 (<010>) and 3 (<310>) at x = 6.2 and 3.1 Å, respectively. These stable and
208 metastable layered structures viewed at right angles to the basal plane are shown in Fig. 4.
209 The overlap between the interfacial tetrahedral sheets at right angles to the basal planes are
210 almost identical for these three structures. The difference between the stable and metastable
211 structures were clear when considering the overlap of octahedral and tetrahedral sheets near

This is a preprint, the final version is subject to change, of the American Mineralogist (MSA)
Cite as Authors (Year) Title. American Mineralogist, in press.
DOI: https://doi.org/10.2138/am-2020-7333

the interface. The stable structures seem to avoid overlap, while the metastable structure overlaps between the tetrahedra and octahedra as shown in Fig. 4. Such overlap would render repulsive interactions owing to the electrostatic interactions among oxygen atoms and among cations.

These interlayer structures were compared to actual pyrophyllite crystals with stacking disorder, and observed using HRTEM (Kogure et al. 2006; Kogure and Kameda 2008). The HRTEM image in Fig. 5 was interpreted as pyrophyllite and observed along [−110]. The dark spots in the tetrahedral sheets and octahedral sheets correspond to a pair of Si tetrahedra and Al octahedra, respectively. The stacking sequence is represented as a black solid line connecting the dark spots, to act as a visual guide. There are three types of interlayer structures. A structure indicated by asterisks in Fig. 5, which correspond to the metastable structures found in our study, is rare. On the other hand, the other two interlayer structures that are abundant in the image correspond to stable structures in our study. Therefore, the occurrence of these three stacking structures in natural pyrophyllite probably corresponds to their stability derived by our simulation.

Frictional forces along six sliding paths

The distance derivative of potential energy profiles provides the frictional force

This is a preprint, the final version is subject to change, of the American Mineralogist (MSA)
Cite as Authors (Year) Title. American Mineralogist, in press.
DOI: https://doi.org/10.2138/am-2020-7333

229 along the sliding paths. The shear stress is plotted in Fig. 6. Assuming that the energy to
230 reduce the potential energy is dissipated via surface phonons (Cieplak et al. 1994), the
231 negative shear stress cannot contribute to the friction (Zhong and Tománek 1990). The
232 positive shear stress increases with increasing normal stress for all sliding paths. The
233 average shear stress, which may correspond to steady-state friction, can be calculated by
234 integrating the positive shear stress along *x* and dividing by the path length. The average
235 shear stress τ as a function of normal stress σ_n is plotted in Fig. 7. The average gradient μ
236 among six paths obtained by fitting a simple linear equation of $\tau = \mu\sigma_n + C$ was $\mu = 0.078$
237 which is consistent within an order of magnitude of that (0.03) measured for atomic-scale
238 friction between a pyrophyllite surface and a silicon nitride Si_3N_4 tip (Bucholz et al. 2012).
239 It should be noted that the shear and normal stresses are the values at the real contact area;
240 therefore, these values are not equal to the macroscopic shear and normal stresses applied
241 in macroscopic experiments. Shear stresses are required even when $\sigma_n = 0$ GPa and a linear
242 relationship can be obtained for all six sliding directions. The differences among sliding
243 directions reflect the degree of overlap of SiO_4 tetrahedra and AlO_6 octahedra during
244 sliding. Shear stresses were smaller than those calculated for muscovite basal planes
245 (Sakuma et al. 2018). The large shear stress for muscovite is due to the strong electrostatic

246 repulsion between positive potassium ions in the interlayer space and cations in tetrahedral
247 sheets during sliding. In contrast, the basal plane of pyrophyllite does not have an interlayer
248 cation, resulting in low shear stresses.

249 A possible uncertainty to compare our results with real material would be the
250 presence of defects and/or isomorphic substitutions of cations which were neglected in our
251 study. We cannot estimate the potential energy change due to the presence of such defects
252 and substitutions without further additional simulations. These effects should be discussed
253 combined with the density of defects and impurities in future works.

254

255 **Implications for macroscopic frictions**

256 **Friction coefficient of basal plane**

257 Most observable macroscopic frictional forces have a linear relationship with
258 applied loads according to Amontons's law (Amontons 1699). This relationship can be
259 interpreted as the change in the real contact area as observed at the μm to mm scale (Abe et
260 al. 2002) and the real contact area A_r can be described as a function of the normal load L as
261 follows (Dieterich and Kilgore 1996).

262

This is a preprint, the final version is subject to change, of the American Mineralogist (MSA)
Cite as Authors (Year) Title. American Mineralogist, in press.
DOI: https://doi.org/10.2138/am-2020-7333

263 $$A_r = \frac{L}{p} \quad (5)$$

264

265 Here p is the indentation hardness of the material. In this expression, the possible finite real
266 contact area at $L = 0$ was ignored. In the previous section, the shear stress at the real contact
267 area was calculated using the DFT method; therefore, macroscopic shear stress τ_{macro} of
268 pyrophyllite can be obtained as follows.

269

270 $$\tau_{\mathrm{macro}} = \frac{A_r}{A}\tau = \frac{A_r}{A}(\mu\sigma_{\mathrm{n}} + \mathrm{C}) = \left(\mu + \frac{\mathrm{C}}{p}\right)\sigma_{n,\mathrm{macro}} \quad (6)$$

271

272 Here, A is the surface area and $\sigma_{n,\,macro}$ is the macroscopic normal stress. This equation was
273 confirmed to be plausible by the analysis of a single-crystal muscovite surface (Sakuma et
274 al. 2018). The macroscopic frictional coefficient $\mu_{macro} = \mu + C/p$ is estimated to be $\mu_{macro} =$
275 0.134 by using $\mu = 0.078$ and $C = 0.182$ GPa for averaging six sliding paths in our
276 simulations and the experimental value of $p = 3.3$ GPa (Zhang et al. 2013). The
277 macroscopic frictional value (0.134) is smaller than those experimentally measured friction
278 coefficients of pyrophyllite gouge (0.276 for wet and 0.375 for dry) (Moore and Lockner
279 2004). The reason for this discrepancy should be the presence of large frictional forces in

This is a preprint, the final version is subject to change, of the American Mineralogist (MSA)
Cite as Authors (Year) Title. American Mineralogist, in press.
DOI: https://doi.org/10.2138/am-2020-7333

experiments among various crystallographic planes (Moore and Lockner 2004; Kawai et al. 2015). Pyrophyllite is a hydrophobic mineral and the effect of water would enhance the preferred orientation of gouge particles rather than the lubrication of adsorbed water.

The friction coefficient of randomly oriented pyrophyllite particles

Here the friction coefficient of simulated gouge was estimated by using a model, schematically shown in Fig. 8. In the shear zone, pyrophyllite particles should have a distribution in the orientation. The orientation of pyrophyllite particles was defined by a unit vector **n** perpendicular to the basal plane as shown in Fig. 8 (A). The external force $\mathbf{F}_{\text{ext}}$ can be decomposed to in-plane $\mathbf{F}_{\text{interlayer}}$ and out-of-plane forces $\mathbf{F}_{\text{normal}}$ for the top pyrophyllite particle as shown in Fig. 8 (C) and (D). Both forces depend on the angles θ and φ as follows in cartesian coordinates.

$$\mathbf{F}_{\text{interlayer}} = |\mathbf{F}_{\text{ext}}|(-\sin^2\theta\cos\varphi\sin\varphi\,,\,1-\sin^2\theta\sin^2\varphi\,,\,-\sin\theta\cos\theta\sin\varphi) \quad (7a)$$

$$\mathbf{F}_{\text{normal}} = |\mathbf{F}_{\text{ext}}|(\sin^2\theta\cos\varphi\sin\varphi\,,\,\sin^2\theta\sin^2\varphi\,,\,\sin\theta\cos\theta\sin\varphi) \quad (7b)$$

The force F_{friction} required to slide the interlayer of pyrophyllite can be estimated by the macroscopic frictional coefficient of 0.134 calculated in this study and by the normal force

This is a preprint, the final version is subject to change, of the American Mineralogist (MSA)
Cite as Authors (Year) Title. American Mineralogist, in press.
DOI: https://doi.org/10.2138/am-2020-7333

297 applied to the basal plane. If the confining pressure P_c is applied on the gouge, the normal
298 force F_{nc} from the confining pressure on the basal plane of pyrophyllite is independent of
299 the orientation. The net normal force F_n was calculated as follows.

300

301 $$F_n = \begin{cases} F_{nc} - |\mathbf{F}_{normal}|, & \text{for } 0 \le \varphi < \pi \\ F_{nc} + |\mathbf{F}_{normal}|, & \text{for } \pi \le \varphi < 2\pi \end{cases} \quad (8)$$

302

303 Here, the direction toward the basal plane was defined to be positive and the direction
304 changes at below and above φ = 180º as observed in Fig. 8 (C) and (D). The interlayer
305 frictional force can be described as follows.

306

307 $$F_{friction} = \mu_{macro} F_n \quad (9)$$

308

309 If the interlayer force $F_{interlayer}$ is larger than the frictional force $F_{friction}$, then interlayer
310 sliding occurs. If the frictional force $F_{friction}$ is larger than the frictional force between the
311 edges of pyrophyllite particles, then sliding should occur at the edge-edge interface. The
312 friction coefficient, except for interlayer sliding, can be calculated from Byerlee's law
313 (Byerlee 1978). We used the friction coefficient of 0.85 for the frictional force $F_{Byerlee}$. The

This is a preprint, the final version is subject to change, of the American Mineralogist (MSA)
Cite as Authors (Year) Title. American Mineralogist, in press.
DOI: https://doi.org/10.2138/am-2020-7333

external forces F_{ext} for randomly oriented pyrophyllite particles were calculated by following the above criterion and the average friction coefficient μ_{gouge} was obtained as follows.

$$\mu_{\text{gouge}} = \frac{1}{N}\sum_{i=1}^{N}\frac{F_{\text{ext}}(i)}{F_{\text{n}}} \qquad (10)$$

Here $F_{ext}(i)$ is the external force of the i-th oriented pyrophyllite, N is the number of differently oriented pyrophyllite particles. The sampled normal vectors **n** of pyrophyllite are plotted in Fig. 8 (B). The figure indicates that the vectors were randomly distributed in space with N = 50,000. Examples of the forces at φ = 90º and 270º are plotted in Fig. 8 (E) and (F), respectively. The net normal force F_n increased and decreased with increasing cos θ at φ = 90º and φ = 270º, respectively. These changes of F_n were because of the presence of $\mathbf{F}_{normal}$ generated by the external force $\mathbf{F}_{ext}$. The friction coefficient of i-th particle $\mu_{gouge}(i)$ was determined using lower force between $|\mathbf{F}_{ext}|$ and $F_{Byerlee}$. The macroscopic coefficient of pyrophyllite gouge calculated by this simple model was μ_{gouge} = 0.203 ± 0.001, which is slightly smaller than 0.276 of preferentially oriented pyrophyllite gouge in wet triaxial experiments (Moore and Lockner 2004) and clearly smaller than Byerlee's law.

This is a preprint, the final version is subject to change, of the American Mineralogist (MSA)
Cite as Authors (Year) Title. American Mineralogist, in press.
DOI: https://doi.org/10.2138/am-2020-7333

331 The difference between the estimated and experimental friction coefficients may imply a
332 difference in the degree of preferred orientation and the presence of other deformation
333 mechanisms which are ignored in this study. From these results, macroscopic friction is
334 strongly related to atomic-scale friction in the interlayer and therefore the crystallographic
335 structure has a large effect on the frictional properties of gouge layers.
336

337 **Acknowledgements**

338 We acknowledge H. Okuda for a discussion on modeling the gouge friction. The DFT
339 calculations were conducted using the Numerical Materials Simulator at NIMS. This work
340 was supported by JSPS KAKENHI grant number 17H05320.
341

342 **References**

343 Abe, S., Dieterich, J.H., Mora, P., and Place, D. (2002) Simulation of the influence of rate-
344 and state-dependent friction on the macroscopic behavior of complex fault zones with
345 the lattice solid model. Pure and Applied Geophysics, 159, 1967–1983.
346 Amiguet, E., Reynard, B., Caracas, R., Van de Moortèle, B., Hilairet, N., and Wang, Y.
347 (2012) Creep of phyllosilicates at the onset of plate tectonics. Earth and Planetary

348 Science Letters, 345–348, 142–150.

349 Amontons, M. (1699) De la resistance cause'e dans les machines. Histoire de l'Académie

350 Royale des Sciences, 206–223.

351 Barone, V., Casarin, M., Forrer, D., Pavone, M., Sambi, M., and Vittadini, A. (2009) Role

352 and effective treatment of dispersive forces in materials: Polyethylene and graphite

353 crystals as test cases. Journal of Computational Chemistry, 30, 934–939.

354 Behnsen, J., and Faulkner, D.R. (2012) The effect of mineralogy and effective normal

355 stress on frictional strength of sheet silicates. Journal of Structural Geology, 42, 49–

356 61.

357 Bengtsson, L. (1999) Dipole correction for surface supercell calculations. Physical Review

358 B, 59, 12301–12304.

359 Bos, B., and Spiers, C.J. (2001) Experimental investigation into the microstructural and

360 mechanical evolution of phyllosilicate-bearing fault rock under conditions favouring

361 pressure solution. Journal of Structural Geology, 23, 1187–1202.

362 Bucholz, E.W., Zhao, X., Sinnott, S.B., and Perry, S.S. (2012) Friction and wear of

363 pyrophyllite on the atomic scale. Tribology Letters, 46, 159–165.

364 Byerlee, J. (1978) Friction of Rocks. Pure and Applied Geophysics, 116, 615–626.

Chen, J., and Spiers, C.J. (2016) Rate and state frictional and healing behavior of carbonate fault gouge explained using microphysical model. Journal of Geophysical Research: Solid Earth, 121, 8642–8665.

Chen, J., Niemeijer, A.R., and Spiers, C.J. (2017) Microphysically derived expressions for rate-and-state friction parameters, a, b, and D_c. Journal of Geophysical Research: Solid Earth, 122, 9627–9657.

Cieplak, M., Smith, E.D., and Robbinst, M.O. (1994) Molecular Origins of Friction: The Force on Adsorbed Layers. Science, 265, 1209–1212.

Dieterich, J.H. (1979) Modeling of rock friction: 1. Experimental results and constituve equations. Journal of Geophysical Research, 84, 2161–2168.

Dieterich, J.H., and Kilgore, B.D. (1996) Imaging surface contacts: power law contact distributions and contact stresses in quartz, calcite, glass and acrylic plastic. Tectonophysics, 256, 219–239.

Garrity, K.F., Bennett, J.W., Rabe, K.M., and Vanderbilt, D. (2014) Pseudopotentials for high-throughput DFT calculations. Computational Materials Science, 81, 446–452.

Giannozzi, P., Baroni, S., Bonini, N., Calandra, M., Car, R., Cavazzoni, C., Ceresoli, D., Chiarotti, G.L., Cococcioni, M., Dabo, I., and others (2009) Q_{UANTUM} ESPRESSO: a

modular and open-source software project for quantum simulations of materials. Journal of Physics: Condensed Matter, 21, 395502.

Giannozzi, P., Andreussi, O., Brumme, T., Bunau, O., Buongiorno Nardelli, M., Calandra, M., Car, R., Cavazzoni, C., Ceresoli, D., Cococcioni, M., and others (2017) Advanced capabilities for materials modelling with QUANTUM ESPRESSO. Journal of Physics:Condensed Matter, 29, 465901.

Grimme, S. (2006) Semiempirical GGA-type density functional constructed with a long-range dispersion correction. Journal of Computational Chemistry, 27, 1787–1799.

Hohenberg, P., and Kohn, W. (1964) Inhomogeneous electron gas. Physical Review, 136, B864–B871.

Horn, H.M., and Deere, D.U. (1962) Frictional Characteristics of Minerals. Géotechnique, 12, 319–335.

Ikari, M.J., Saffer, D.M., and Marone, C. (2007) Effect of hydration state on the frictional properties of montmorillonite-based fault gouge. Journal of Geophysical Research, 112, B06423.

Jefferies, S.P., Holdsworth, R.E., Wibberley, C.A.J., Shimamoto, T., Spiers, C.J., Niemeijer,

399 A.R., and Lloyd, G.E. (2006) The nature and importance of phyllonite development in
400 crustal-scale fault cores: An example from the Median Tectonic Line, Japan. Journal
401 of Structural Geology, 28, 220–235.
402 Katayama, I., Kubo, T., Sakuma, H., and Kawai, K. (2015) Can clay minerals account for
403 the behavior of non-asperity on the subducting plate interface? Progress in Earth and
404 Planetary Science, 2, 30.
405 Kawai, K., Sakuma, H., Katayama, I., and Tamura, K. (2015) Frictional characteristics of
406 single and polycrystalline muscovite and influence of fluid chemistry. Journal of
407 Geophysical Research B: Solid Earth, 120, 6209–6218.
408 Kogure, T., and Kameda, J. (2008) High-resolution TEM and XRD simulation of stacking
409 disorder in 2:1 phyllosilicates. Zeitschrift für Kristallographie - Crystalline Materials,
410 223, 69–75.
411 Kogure, T., Jige, M., Kameda, J., Yamagishi, A., Miyawaki, R., and Kitagawa, R. (2006)
412 Stacking structures in pyrophyllite revealed by high-resolution transmission electron
413 microscopy (HRTEM). American Mineralogist, 91, 1293–1299.
414 Kohn, W., and Sham, L.J. (1965) Self-consistent equations including exchange and
415 correlation effects. Physical Review, 140, 1133–1138.

Lee, J.H., and Guggenheim, S. (1981) Single crystal X-ray refinement of pyrophyllite-1*Tc*. American Mineralogist, 66, 350–357.

Mariani, E., Brodie, K.H., and Rutter, E.H. (2006) Experimental deformation of muscovite shear zones at high temperatures under hydrothermal conditions and the strength of phyllosilicate-bearing faults in nature. Journal of Structural Geology, 28, 1569–1587.

Monkhorst, H.J., and Pack, J.D. (1976) Special points for Brillouin-zone integrations. Physical Review B, 13, 5188–5192.

Moore, D.E., and Lockner, D.A. (2004) Crystallographic controls on the frictional behavior of dry and water-saturated sheet structure minerals. Journal of Geophysical Research, 109, 1–16.

Moore, D.E., and Lockner, D.A. (2007) Friction of the Smectite Clay Montmorillonite, A review and interpretation of data. In T.H. Dixon and J.C. Moore, Eds., The Seismogenic Zone of Subduction Thrust Faults pp. 317–345. Columbia University Press.

Morrow, C.A., Moore, D.E., and Lockner, D.A. (2000) The effect of mineral bond strength and adsorbed water on fault gouge frictional strength. Geophysical Research Letters, 27, 815–818.

433 Morrow, C.A., Moore, D.E., and Lockner, D.A. (2017) Frictional Strength of Wet and Dry
434 Montmorillonite. Journal of Geophysical Research: Solid Earth, 122,
435 doi:10.1002/2016JB013658.
436 Okuda, H., Kawai, K., and Sakuma, H. (2019) First-principles investigation of frictional
437 characteristics of brucite: An application to its macroscopic frictional characteristics.
438 Journal of Geophysical Research: Solid Earth, 124, 10423–10443.
439 Perdew, J.P., Burke, K., and Ernzerhof, M. (1996) Generalized gradient approximation
440 made simple. Physical Review Letters, 77, 3865–3868.
441 Ruina, A. (1983) Slip instability and state variable friction laws. Journal of Geophysical
442 Research: Solid Earth, 88, 10359–10370.
443 Sakuma, H. (2013) Adhesion energy between mica surfaces: Implications for the frictional
444 coefficient under dry and wet conditions. Journal of Geophysical Research: Solid
445 Earth, 118, 6066–6075.
446 Sakuma, H., and Suehara, S. (2015) Interlayer bonding energy of layered minerals:
447 Implication for the relationship with friction coefficient. Journal of Geophysical
448 Research B: Solid Earth, 120, 2212–2219.
449 Sakuma, H., Otsuki, K., and Kurihara, K. (2006) Viscosity and lubricity of aqueous NaCl

450 solution confined between mica surfaces studied by shear resonance measurement.
451 Physical Review Letters, 96, 046104.
452 Sakuma, H., Kondo, T., Nakao, H., Shiraki, K., and Kawamura, K. (2011) Structure of
453 hydrated sodium ions and water molecules adsorbed on the mica/water interface. The
454 Journal of Physical Chemistry C, 115, 15959–15964.
455 Sakuma, H., Tachi, Y., Yotsuji, K., Suehara, S., Arima, T., Fujii, N., Kawamura, K., and
456 Honda, A. (2017) Stability of montmorillonite edge faces studied using first-principles
457 calculations. Clays and Clay Minerals, 65, 252–272.
458 Sakuma, H., Kawai, K., Katayama, I., and Suehara, S. (2018) What is the origin of
459 macroscopic friction? Science Advances, 4, eaav2268.
460 Schwarz, U.D., and Hölscher, H. (2016) Exploring and explaining friction with the
461 Prandtl-Tomlinson model. ACS Nano, 10, 38–41.
462 Shea, W.T., and Kronenberg, A.K. (1993) Strength and anisotropy of foliated rocks with
463 varied mica contents. Journal of Structural Geology, 15, 1097–1121.
464 Tetsuka, H., Katayama, I., Sakuma, H., and Tamura, K. (2018) Effects of humidity and
465 interlayer cations on the frictional strength of montmorillonite. Earth, Planets and
466 Space, 70, 56.

Weck, P.F., Kim, E., and Jové-Colón, C.F. (2015) Relationship between crystal structure and thermo-mechanical properties of kaolinite clay: beyond standard density functional theory. Dalton Transactions, 44, 12550–12560.

Wintsch, R.P., Christoffersen, R., and Kronenberg, A.K. (1995) Fluid-rock reaction weakening of fault zones. Journal of Geophysical Research, 100, 13021–13032.

Zhang, J., Hu, L., Pant, R., Yu, Y., Wei, Z., and Zhang, G. (2013) Effects of interlayer interactions on the nanoindentation behavior and hardness of 2:1 phyllosilicates. Applied Clay Science, 80–81, 267–280.

Zhong, W., and Tománek, D. (1990) First-principles theory of atomic-scale friction. Physical Review Letters, 64, 3054–3057.

This is a preprint, the final version is subject to change, of the American Mineralogist (MSA)
Cite as Authors (Year) Title. American Mineralogist, in press.
DOI: https://doi.org/10.2138/am-2020-7333

Revision 1

List of figure captions

Fig. 1 (A) Side view of two pyrophyllite layers in the supercell. A sliding plane was placed between the layers. The thin black line indicates the supercell. (B) Top view of the six sliding directions from 1 to 6 between the pyrophyllite layers. Tetrahedral SiO_4 sheets on the interface of the top layer are only shown here. The end of each arrow indicates the crystallographic equivalent position from the initial position by sliding.

Fig. 2 Structures of SiO_4 tetrahedral sheets at the interface of the sliding plane along path 1 at (A) $x = 0$, (B) $x = 10/19\ L$, and (C) $x = L$. Triangles indicate the SiO_4 tetrahedra in the top pyrophyllite layer and are used as a guide in order to determine the displacement. (D) Definition of the z axis perpendicular to the basal plane. (E) The interlayer energies calculated at various x and z positions. Lines are fitting curves to the calculated values.

Fig. 3 Potential energy changes along six sliding paths as a function of normal stresses from 0 to 10.7 GPa. Solid lines are fitted curves and can be described by a linear combination of sine and cosine functions.

This is a preprint, the final version is subject to change, of the American Mineralogist (MSA)
Cite as Authors (Year) Title. American Mineralogist, in press.
DOI: https://doi.org/10.2138/am-2020-7333

Fig. 4 A comparison of stable and metastable structures obtained from this study. The overlap of interfacial tetrahedral sheets (top) and tetrahedral-octahedral sheets (bottom) are shown for the structures along path 1 at three minimum potential energies.

Fig. 5 Comparison of three stacking structures predicted by our simulations and the observations of natural pyrophyllite by using HRTEM (Kogure et al. 2006) with permission from the American Mineralogical Society. A solid line was added on the HRTEM image as a visual guide for the eye. The asterisks indicate a rare stacking structure found by the HRTEM.

Fig. 6 Shear stress calculated by the displacement derivative of potential energy along six sliding paths. Negative shear stresses were not used for deriving average shear stress by assuming the dissipation of phonon energy.

Fig. 7 Shear stress τ as a function of normal stress σ_n at the real contact area. Lines near the symbols indicate the best-fit linear equations to the calculated values. For comparison, the results of muscovite (Sakuma et al. 2018) are plotted as solid lines.

This is a preprint, the final version is subject to change, of the American Mineralogist (MSA)
Cite as Authors (Year) Title. American Mineralogist, in press.
DOI: https://doi.org/10.2138/am-2020-7333

513

514 Fig. 8 (A) Definition of the unit vector **n** perpendicular to the basal plane of a pyrophyllite
515 particle. The angles θ and φ are defined as shown in the figure. The direction of shear is
516 parallel to the y_1 axis. (B) Sampled **n** for calculating the frictional force of randomized
517 oriented pyrophyllite particles. One dot corresponds to one **n** vector. The number of
518 sampling N was 50,000. Examples of the external interlayer force $F_{\text{interlayer}}$ to slide along the
519 basal plane generated by the external force F_{ext} at (C) φ = 90º and (D) φ = 270º. Calculated
520 forces and friction coefficients of gouge at (E) φ = 90º and (F) φ = 270º. Here all forces on
521 the basal plane of pyrophyllite applied by confining pressure were normalized by external
522 normal force F_{nc}.

523

524 Table 1. Calculated and experimental lattice constants of pyrophyllite.

Mineral	Lattice constants	Calculated lattice constants by PBE + D2	Experimental results (Lee and Guggenheim 1981)
Pyrophyllite	*a*	5.175 Å (+0.3%)	5.160
	b	8.989 Å (+0.3%)	8.966
	c	9.356 Å (+0.1%)	9.347
	α	90.97º (−0.2%)	91.180
	β	100.58º (+0.1%)	100.460
	γ	89.83º (+0.2%)	86.640

525

This is a preprint, the final version is subject to change, of the American Mineralogist (MSA)
Cite as Authors (Year) Title. American Mineralogist, in press.
DOI: https://doi.org/10.2138/am-2020-7333

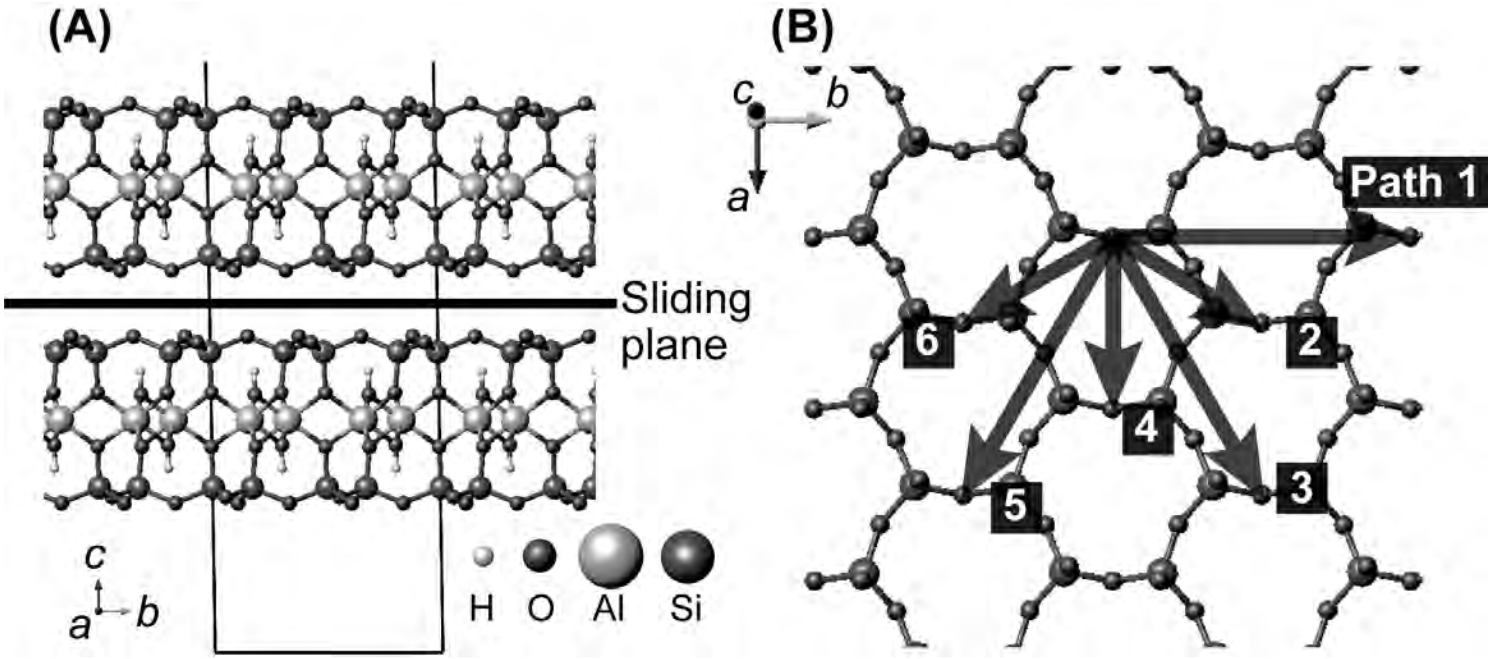

Figure 1

This is a preprint, the final version is subject to change, of the American Mineralogist (MSA)
Cite as Authors (Year) Title. American Mineralogist, in press.
DOI: https://doi.org/10.2138/am-2020-7333

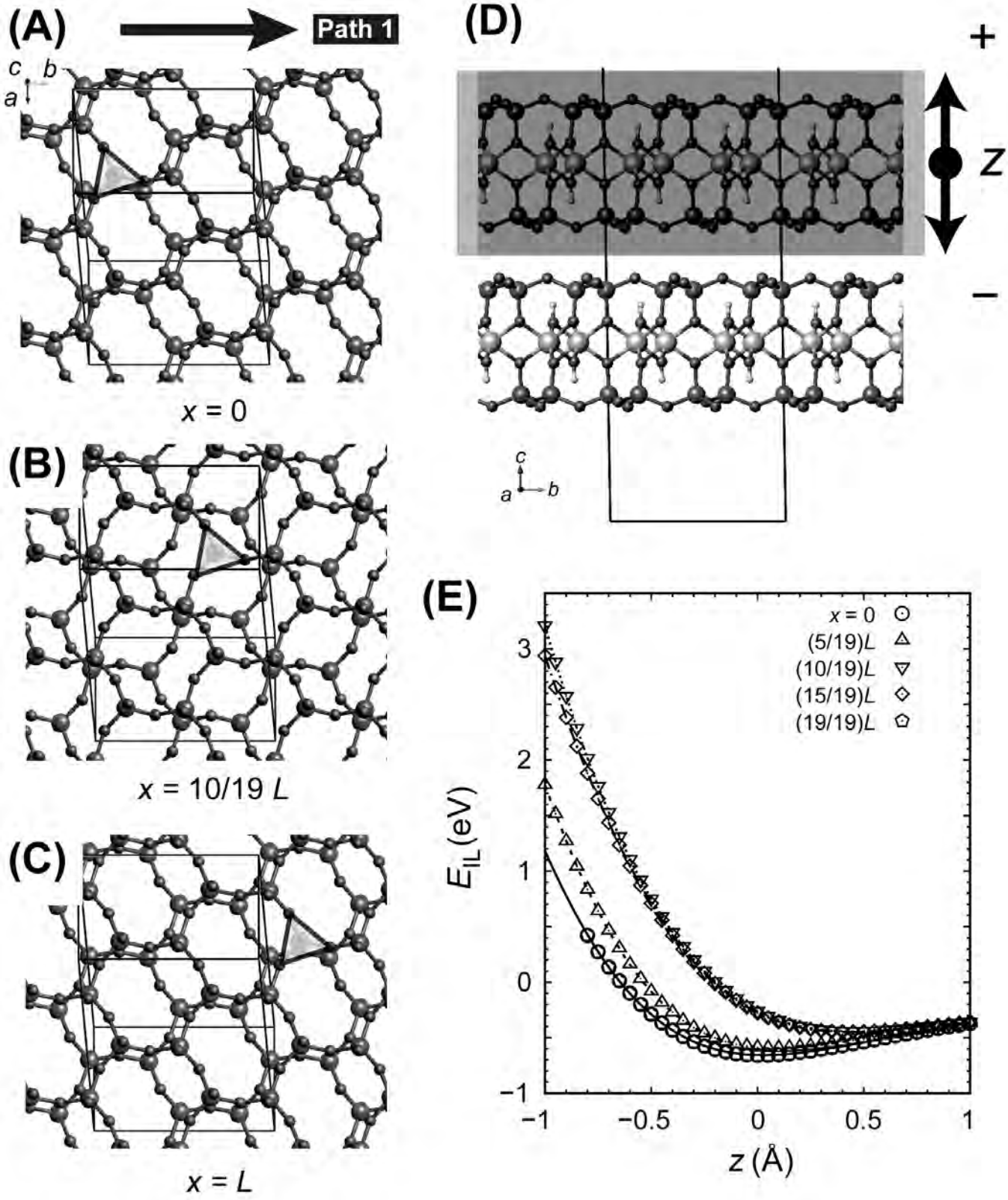

Figure 2

This is a preprint, the final version is subject to change, of the American Mineralogist (MSA)
Cite as Authors (Year) Title. American Mineralogist, in press.
DOI: https://doi.org/10.2138/am-2020-7333

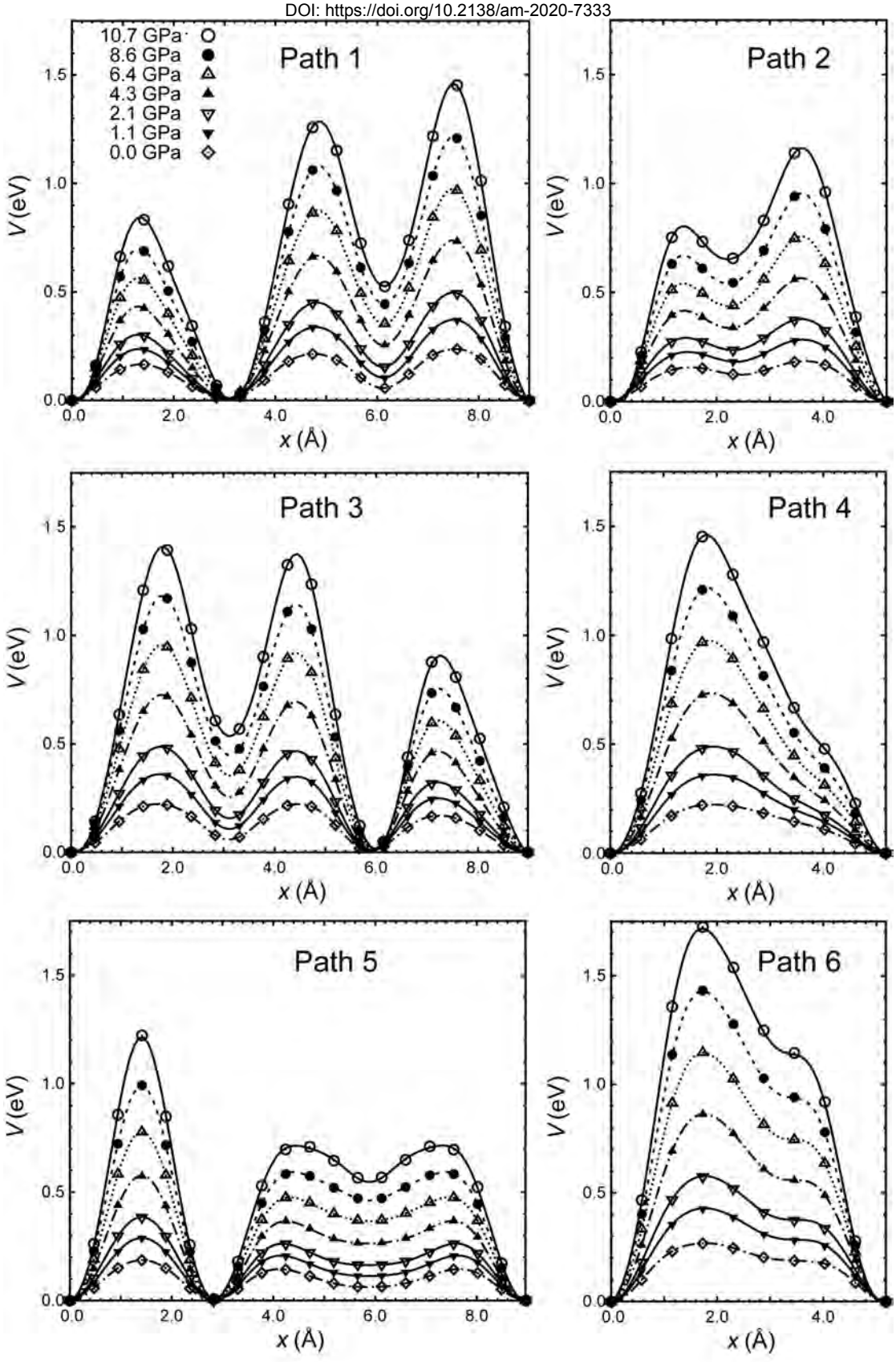

Figure 3

This is a preprint, the final version is subject to change, of the American Mineralogist (MSA)
Cite as Authors (Year) Title. American Mineralogist, in press.
DOI: https://doi.org/10.2138/am-2020-7333

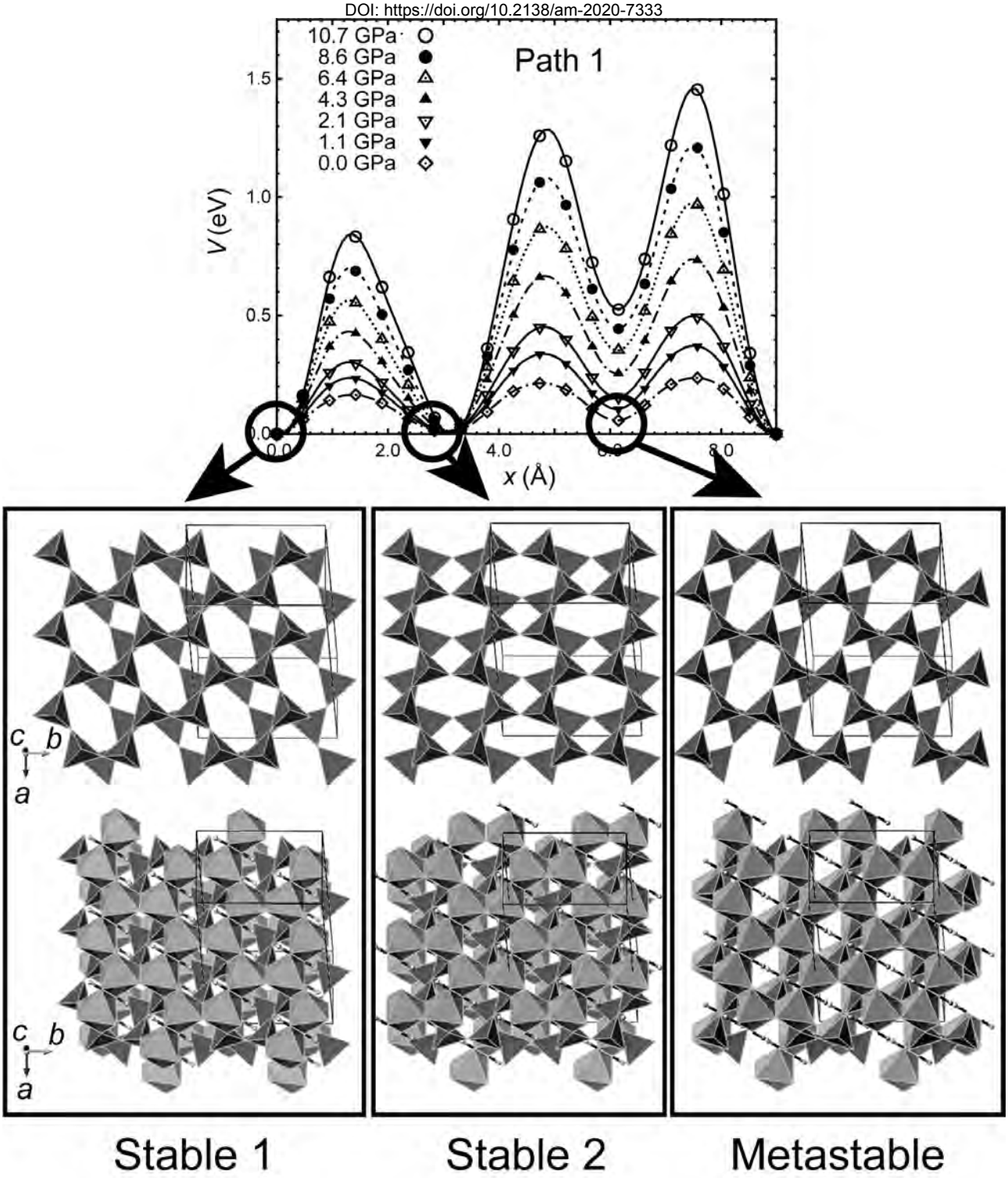

Figure 4

This is a preprint, the final version is subject to change, of the American Mineralogist (MSA)
Cite as Authors (Year) Title. American Mineralogist, in press.
DOI: https://doi.org/10.2138/am-2020-7333

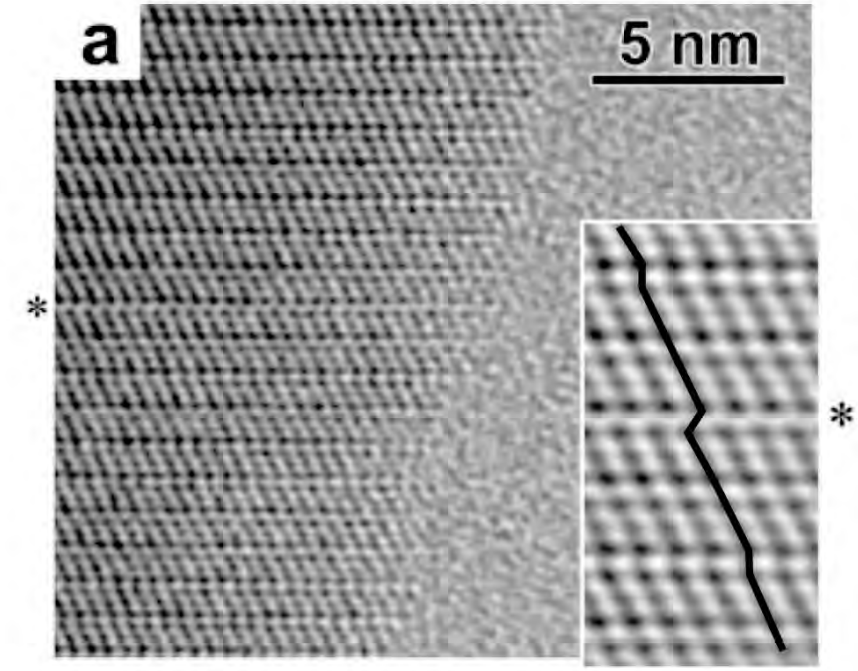

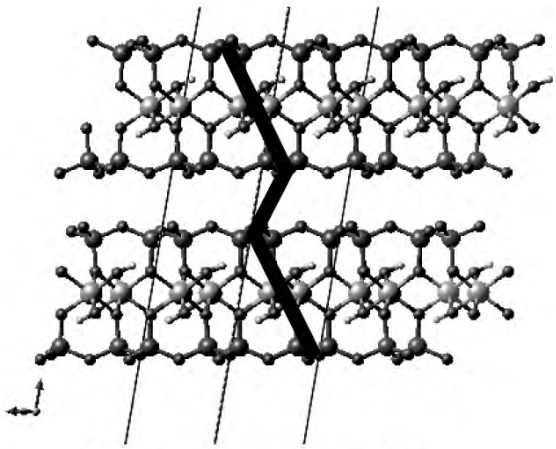

Metastable

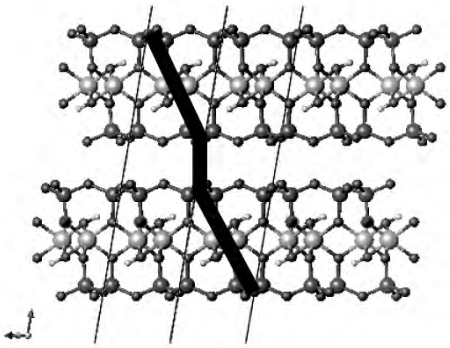

Stable 1

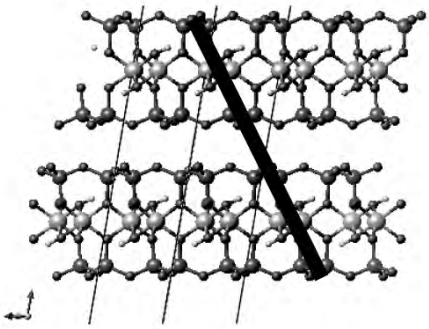

Stable 2

Figure 5

This is a preprint, the final version is subject to change, of the American Mineralogist (MSA)
Cite as Authors (Year) Title. American Mineralogist, in press.
DOI: https://doi.org/10.2138/am-2020-7333

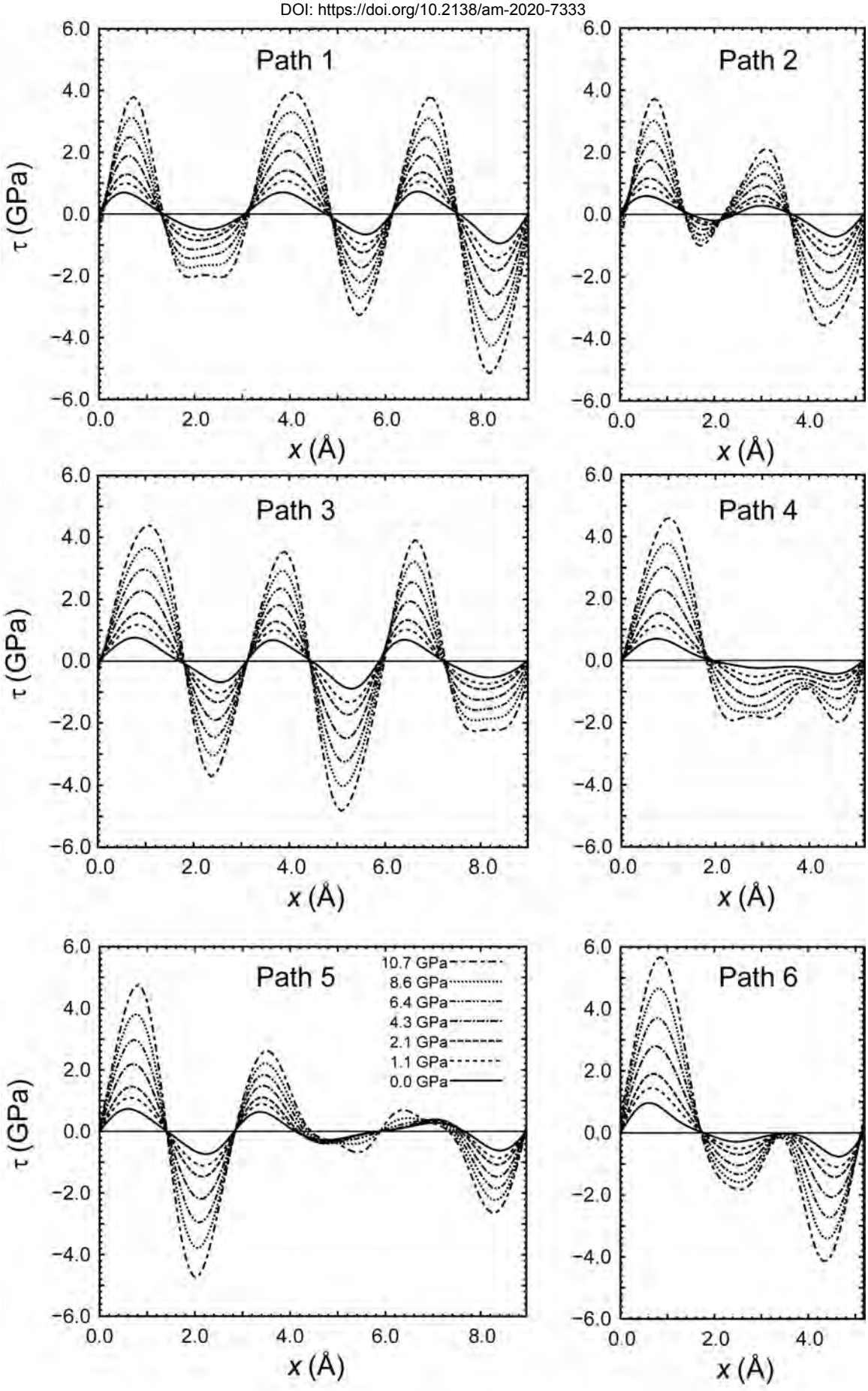

Figure 6

This is a preprint, the final version is subject to change, of the American Mineralogist (MSA)
Cite as Authors (Year) Title. American Mineralogist, in press.
DOI: https://doi.org/10.2138/am-2020-7333

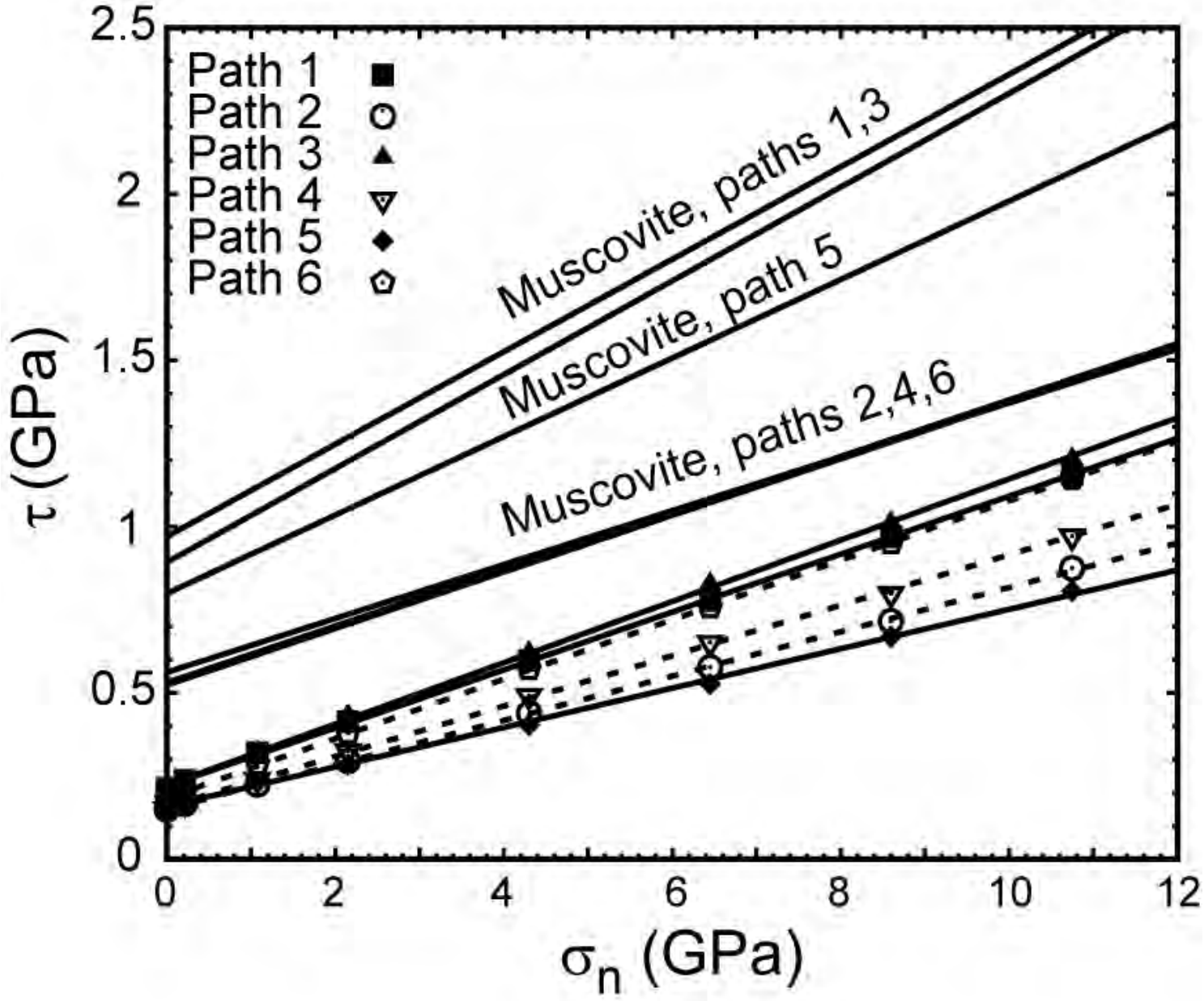

Figure 7

This is a preprint, the final version is subject to change, of the American Mineralogist (MSA)
Cite as Authors (Year) Title. American Mineralogist, in press.
DOI: https://doi.org/10.2138/am-2020-7333

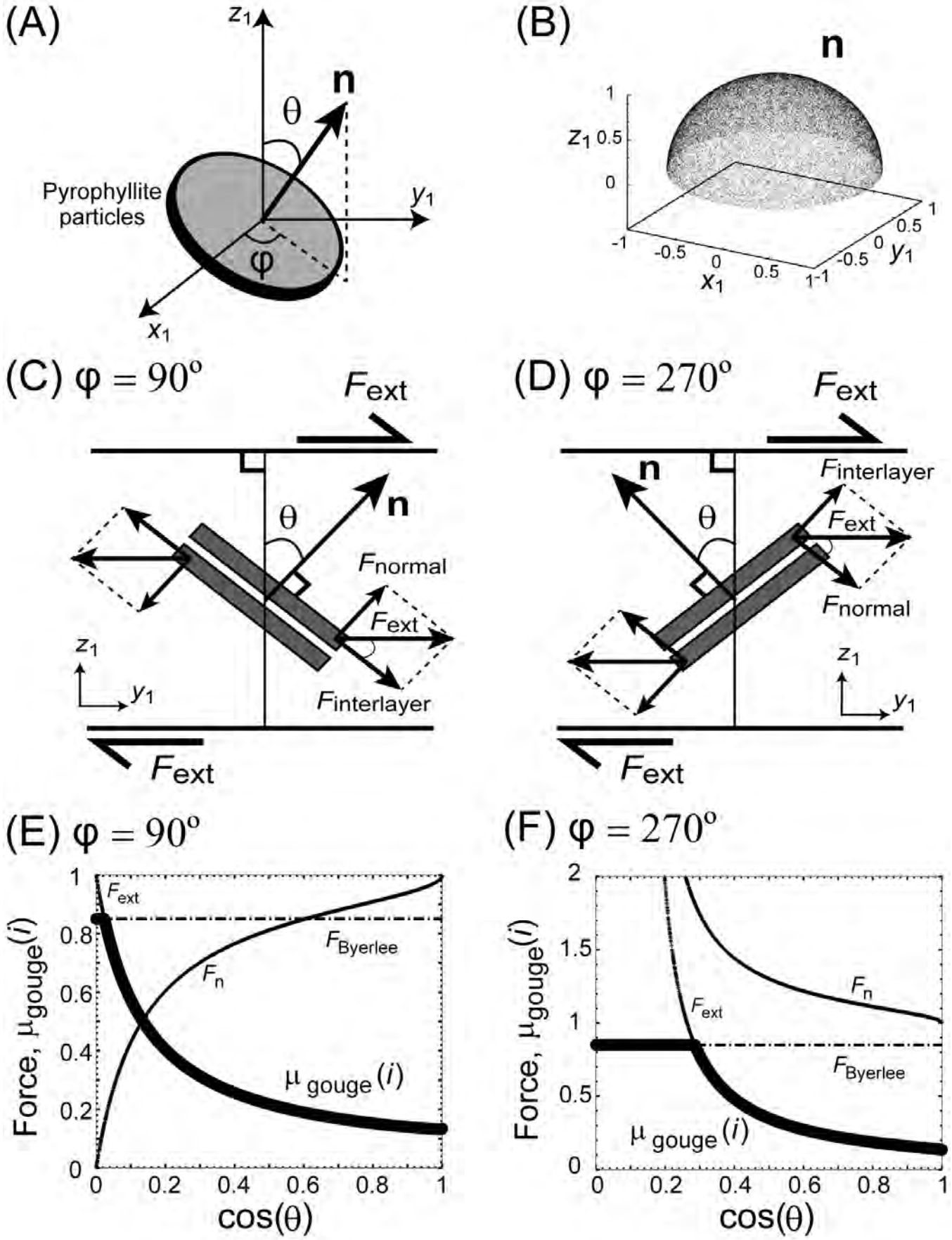

Figure 8